The polar ice caps of Mars

Ralf Greve　北海道大学　低温科学研究所

Both Martian polar regions are covered by prominent ice caps. Similar to snow on Earth, the seasonal caps are extended layers of CO_2 frost which grow and shrink over the seasons. In the respective summer season, much smaller permanent caps remain, which are underlain by 3 km high topographic domes termed as polar layered deposits. The polar layered deposits consist mainly of H_2O ice and have formed by exchange of water with the atmosphere over at least millions of years. Alternating layers of clear and dusty ice, which are exposed in surface troughs and close to the margin, indicate a complex climatic history of Mars driven by quasi-periodic changes of orbital elements, similar to the Milankovitch cycles on Earth. Likely present-day glacial flow velocities are of the order of 0.1–1 mma^{-1}, the north polar deposits being more dynamic than the southern ones due to higher surface temperatures. Basal temperatures are far below the pressure melting point, with the possible exception of geothermally active areas under the ice.

1. Geological setting and composition

One of the most prominent features of the Martian surface are the polar ice caps. In each winter season, the northern and southern polar regions of Mars become frosted equator-wards until beyond the 55th parallel. This seasonal cover consists of some ten centimeters to meters of frozen CO_2 (dry ice), which forms from atmospheric CO_2 in the low polar winter temperatures of about 145 K (Forget 1998). This process, which therefore has two maxima during the Martian year, absorbs up to one third of the entire atmosphere, leading to distinct seasonal variations of the air pressure. However, the southern winter pressure minimum is more pronounced than the northern winter counterpart. This is so because the eccentricity of the Martian orbit around the sun is relatively large ($e_{\mathrm{Mars}}=0.093$, compared to $e_{\mathrm{Earth}}=0.017$), the perihelion being reached during the southern summer (like on Earth), and as a consequence the contrast between summer and winter is larger in the southern hemisphere than in the northern hemisphere.

During the respective summer, the largest part of the dry ice sublimes back into the atmosphere; however, a certain residual cap always survives. In the north polar region, this residual ice is centered near the pole with a diameter of about 1000 km. By contrast, in the south polar region, the residual ice cover is substantially smaller; it is centered about 200 km away from the pole with a diameter of 300–500 km. The thicknesses of the residual caps (also termed "permanent caps") are not well constrained; however, most likely they are essentially surface features like the seasonal caps. The north polar permanent cap consists of H_2O ice (Kieffer et al. 1976), whereas in the south at least the cover of the permanent cap is CO_2 (Kieffer 1979, Paige et al. 1990). However, more recent findings indicate that the CO_2 ice is only a thin surface layer above H_2O ice, and that the main volatile component of the south polar cap is H_2O ice like in the north (Hvidberg 2005).

The residual caps are underlain by massive topographic structures known as the polar layered deposits (Thomas et al. 1992), which will be referred to as PLDs in the following. The relationship of seasonal caps, permanent caps and PLDs is illustrated in Fig. 1. Shaded relief maps of the north and south polar regions are shown in Fig. 2 along with summer images of the permanent caps. Evidently, the north polar layered deposits (NPLD) and the permanent cap are co-extensive, whereas the south polar layered deposits (SPLD) occupy a much larger area than the permanent cap. It is striking that the overall shape of the NPLD is quite regular and smooth, whereas the

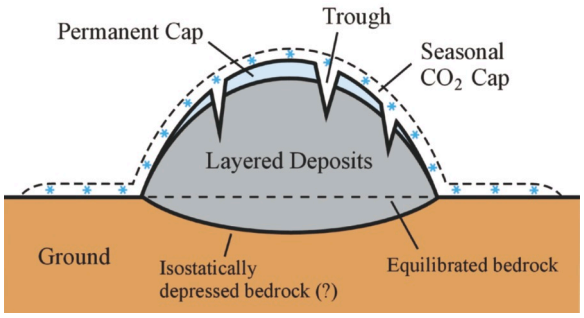

Figure 1: Schematical representation of the seasonal cap, permanent cap and underlying layered deposits for the north polar region of Mars. In the south polar region, the situation is essentially the same; however, the areal extent of the permanent cap is much smaller than that of the layered deposits. The vertical scale is exaggerated by about a factor 150 for the layered deposits, by an unknown factor for the permanent cap and by about a factor 50000 for the seasonal cap.

SPLD appear much more rugged, and the margin of the latter is much more difficult to determine than that of the former. This indicates a less active interaction between the SPLD and the atmosphere and/or less glacial flow of the SPLD than for the NPLD, in agreement with the lower surface temperatures in the south polar region and the larger number of craters on the SPLD (Herkenhoff and Plaut 2000).

Elevation data from the Mars Orbiter Laser Altimeter (MOLA) of the Mars Global Surveyor space probe show that both the NPLD and SPLD raise by approx. 3 km about the surrounding terrain (Zuber et al. 1998, Smith et al. 1999). This rules out CO_2 ice as a major constituent, because such a massive topographic dome of CO_2 ice would be too soft to be stable over glaciological time-scales (Nye et al. 2000). It is therefore generally accepted that the PLDs consist mainly of H_2O ice, with an unknown admixture of dust and possibly small amounts of CO_2 ice. The present volume of the NPLD is approximately $1.2\pm0.2\times10^6$ km^3 which is a bit less than half the volume of the Greenland ice sheet and corresponds to a 7.5 m thick planetwide water layer. The uncertainty arises from the unknown basal topography and possible isostatic deflection of the ground, as indicated in Fig. 1. Due to the more rugged topography and less well defined margins, the volume of the SPLD is more difficult to estimate, but very recent subsurface radar soundings have provided the value $1.6\pm0.2\times10^6$ km^3 (Plaut et al. 2007). The PLDs are therefore important reservoirs for the water cycle of the Martian atmosphere.

An intriguing feature of the Martian PLDs is the presence of large chasmata and smaller troughs which

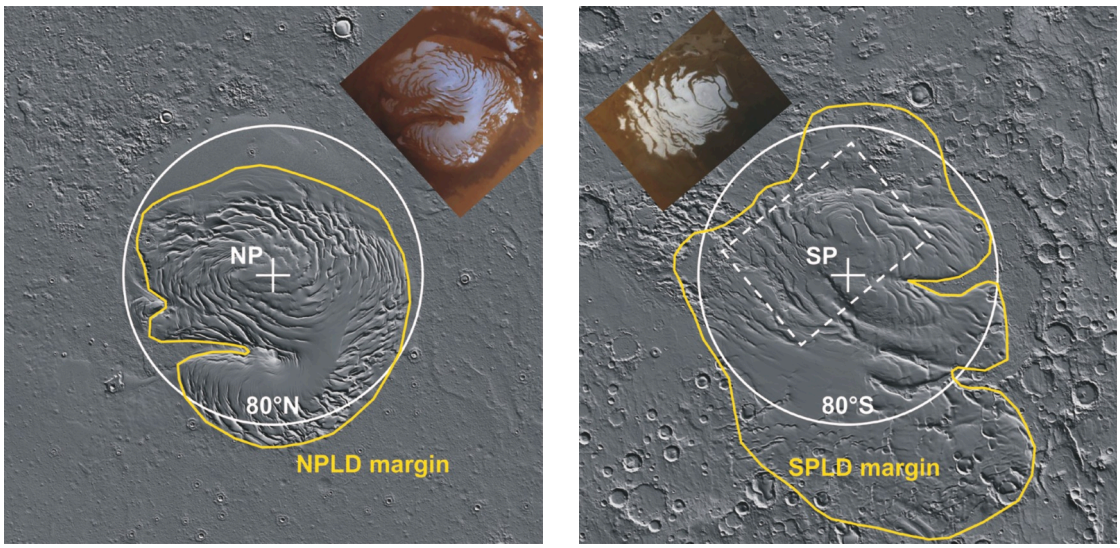

Figure 2: Shaded relief maps of the north (left panel) and south (right panel) polar regions, constructed from Mars Orbiter Laser Altimeter (MOLA) data (image credit: MOLA science team/NASA GSFC). The approximate margins of the north/south polar layered deposits (NPLD/SPLD), the north and south poles (NP/SP) and the parallels 80°N/S are indicated. Insets: Mars Orbiter Camera (MOC) summer images of the residual ice (image refs.: PIA02800 and PIA02393, NASA/Planetary Photojournal; credit: NASA/JPL/MSSS). The location of the MOC images relative to the relief maps is evident for the north polar region, whereas it is indicated by the dashed white line for the south polar region.

have no counterpart in terrestrial ice sheets. They are clearly visible in Fig. 2. The chasmata (Chasma Boreale in the north, Chasma Australe and the two-branch system Promethei/Ultimum Chasma in the south) cut hundreds of kilometers from the margins into the PLDs, while the troughs are organized in patterns which spiral outward from the respective centers. The spiralling direction is counterclockwise for the NPLD and clockwise for the SPLD. While this raises notions of a connection with katabatic winds influenced by the Coriolis force, the origin of the spiralling trough patterns is still a matter of debate (Hvidberg 2005).

2. Polar ice caps and climate

Motivated by NASA's science strategy for Mars exploration to "follow the water", from now on only the PLDs will be discussed, and the distinction between permanent caps (surface features) and PLDs (underlying volume features) will be given up, so that the permanent caps will be considered as parts of the PLDs. Similar to the situation on Earth, the Martian PLDs are active components of the climate system which interact with the atmosphere thermally, orographically and by condensation and sublimation processes of water vapour. Their present topographies are the result of the climatic history over at least the last millions of years.

On time-scales of 10^5–10^6 years, Mars has experienced large periodic changes of the orbital elements obliquity, eccentricity and equinox precession. These changes impact on the Martian climate. The obliquity determines the latitudinal distribution of solar insolation. The eccentricity determines the magnitude of the asymmetry of insolation with season, and the equinox precession determines the timing of the asymmetry of solar insolation with season. On Earth, the so-called Milankovitch cycles of much weaker orbital changes with periods of 20, 40 and 100 ka are considered driving forces for climate variations like the glacial/interglacial cycles. It can, therefore, be expected that the main Martian $\pm 10°$ obliquity cycles with periods of 125 ka and 1.3 Ma and the secular shift from high to low average obliquities at 4–5 Ma ago (Laskar et al. 2004, shown in Fig. 3) have significant impacts on the climate and the PLDs due to large insolation changes in the polar regions.

This idea is supported by the presence of light-dark layers in the PLDs, which are exposed in the surface troughs and close to the margins (Fig. 4), and which are actually the reason for the term "polar *layered* deposits". These layers indicate a strongly varying dust content of the ice due to varying climatic conditions in the past. During periods of high obliq-

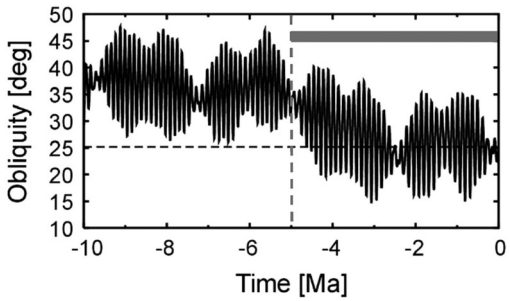

Figure 3: Martian obliquity for the last 10 Ma (Laskar et al. 2004). The grey bar indicates the most recent 5-Ma period with relatively low average obliquity, which favours the formation of polar deposits.

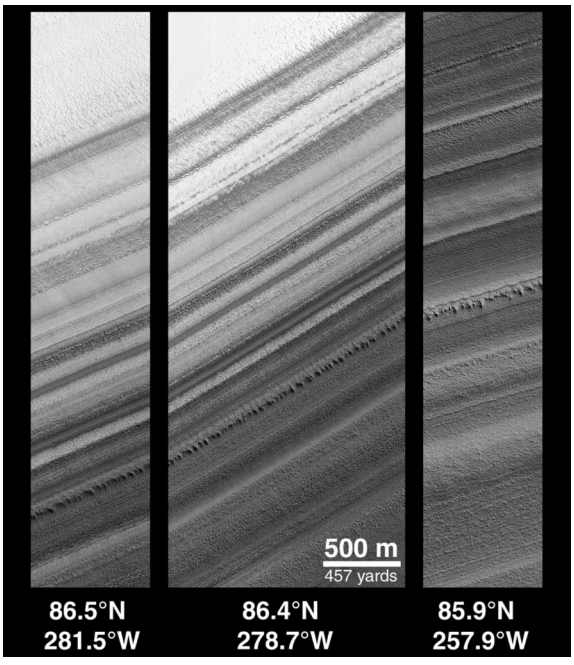

Figure 4: North polar layers in the same trough. Three Mars Orbiter Camera (MOC) images show the fine-structured layering, visible down to the the resolution limit. The left and right images are separated by a distance of more than 100 kilometers. (Image ref.: PIA02070, NASA/Planetary Photojournal; credit: NASA/JPL/MSSS.)

uities, insolation in the polar regions is large, which entails higher sublimation rates of superficial ice of the PLDs and probably of permafrost in the ground. This may lead to the formation of a thicker and dustier atmosphere, so that dust accumulates on the PLDs. By contrast, during periods of low obliquities, the atmosphere is thin and dust deposition is low, so that clean ice forms at the surface of the PLDs. Along this line of reasoning, Head et al. (2003) suggested that Mars experienced "ice ages" during periods of high obliquity like that from about 2.1 to 0.4 Ma ago (with obliquity maxima of $\approx 35°$). These ice ages are supposedly characterized by warmer polar climates, enhanced mass loss of the PLDs due to sublimation and the formation of meters-thick ice deposits equatorward to approximately 30°N/S.

3. Glacial flow

3.1 Viscosity of polycrystalline ice

Ice in natural large ice bodies on Earth, Mars and elsewhere consists of zillions of individual crystals. As long as the orientation of these crystals is randomly distributed, the macroscopic behaviour of the polycrystalline aggregate will be isotropic. On long timescales and for low temperatures (below approximately −10°C), polycrystalline ice responds to applied stresses by *secondary creep*, which can be described by a non-linear viscous flow law [for more details, see Greve (2006), and references therein]. The viscosity η reads

$$\eta(T', \sigma, d)=\frac{1}{2EA(T')}\frac{d^p}{\sigma^{n-1}}, \tag{1}$$

or, equivalently,

$$\eta(T', \delta, d)=\frac{E_s B(T')}{2}\frac{d^{p/n}}{\delta^{1-1/n}}. \tag{2}$$

In Eq. (1), the rate factor $A(T')$ depends on the temperature relative to pressure melting $T'=T-T_m+T_0$ (T: absolute temperature, $T_m=T_0-\beta P$: pressure melting point, P: pressure, $\beta=9.8\times10^{-2}$ KMPa^{-1}: Clausius-Clapeyron constant, $T_0=273.16$K: melting point at zero pressure) via the Arrhenius law

$$A(T')=A_0 e^{-Q/RT'}, \tag{3}$$

where A_0 is the pre-exponential constant, Q the activation energy and $R=8.314$ J mol^{-1} K^{-1} the universal gas constant. The flow enhancement factor E is equal to unity for pure ice, and can be set to values deviating from unity in order to account roughly for effects of impurities and/or anisotropy. Further, $\sigma=[\mathrm{tr}(\mathbf{t}^{\mathrm{D}})^2/2]^{1/2}$ is the effective stress ($\mathbf{t}^{\mathrm{D}}$: deviatoric stress tensor, tr : trace operator), n is the stress exponent, d is the grain size and p is the grain-size exponent. In Eq. (2), $B(T')=[A(T')]^{-1/n}$ is the associated rate factor, $E_s=E^{-1/n}$ the stress enhancement factor and $\delta=(\mathrm{tr}\mathbf{D}^2/2)^{1/2}$ the effective strain rate ($\mathbf{D}=$ symgrad $\mathbf{v}$: strain-rate tensor, symmetrized gradient of the velocity $\mathbf{v}$).

For terrestrial ice sheets, ice caps and glaciers, it is commonly accepted that the deformation processes in the polycrystalline aggregate are dominated by grain-size-independent dislocation creep, so that the the grain-size exponent is $p=0$. Further, the well-established *Glen's flow law* uses the stress exponent $n=3$, and for the temperature range $T'\leq263$ K the pre-exponential constant $A_0=3.985\times10^{-13}$ s^{-1} Pa^{-3} and the activation energy $Q=60$ kJ mol^{-1} (Paterson 1994). However, for the very low temperature and strain-rate conditions expected in the Martian PLDs, it is not clear whether dislocation creep is still the predominant creep mechanism. Grain-size-dependent mechanisms like grain-boundary sliding may become favoured instead, and alternative flow laws with $p\neq0$ have therefore been suggested [again, it is referred to Greve (2006) for more details]. This poses a substantial uncertainty for efforts to simulate the flow field of the Martian PLDs.

3.2 Model equations

The thermomechanical problem of gravity-driven flow of large ice bodies is governed by the balance equations of mass, momentum and energy (e.g. Hutter 1983). For an incompressible medium, which holds for ice in good approximation, the mass balance (continuity equation) reads

$$\mathrm{div}\,\mathbf{v}=\mathbf{0}. \tag{4}$$

For evolving ice bodies, it is convenient to vertically integrate the continuity equation. This yields the ice-thickness (H) equation

$$\frac{\partial H}{\partial t} = -\mathrm{div}\,\mathbf{Q} + a_s - a_b, \tag{5}$$

where $\mathbf{Q}$ is the volume flux (vertically integrated horizontal velocity), and a_s and a_b are the mass balances at the surface (positive for supply) and the bottom (positive for loss), respectively. The momentum balance yields with the viscosity (2) the Stokes equation

$$-\mathrm{grad}\,P + \mathrm{div}[\eta(\mathrm{grad}\,\mathbf{v} + (\mathrm{grad}\,\mathbf{v})^{\mathrm{T}})] + \rho\mathbf{g} = \mathbf{0} \tag{6}$$

(ρ: ice density, $\mathbf{g}$: vectorial gravity acceleration), in which the acceleration term $\rho \mathrm{d}\mathbf{v}/\mathrm{d}t$ has been neglected due to the very low flow velocities to be expected. From the energy balance, Fourier's law of heat conduction

$$\mathbf{q} = -\kappa(T)\mathrm{grad}\,T \tag{7}$$

($\mathbf{q}$: heat flux, κ: heat conductivity) and the caloric equation of state

$$u = \int_{T_0}^{T} c(\bar{T})\,d\bar{T} \tag{8}$$

(u: specific internal energy, c: specific heat), the temperature-evolution equation

$$\rho c\left(\frac{\partial T}{\partial t} + \mathbf{v}\cdot\mathrm{grad}\,T\right) = \mathrm{div}(\kappa\,\mathrm{grad}\,T) + 4\eta\delta^2 + r \tag{9}$$

results. In this relation, the production term $4\eta\delta^2$ is the strain heating, and the source term r denotes the volumetric heating due to radiation and tidal dissipation. Explicit representations of the heat conductivity κ and the specific heat c, which also include the influence of mixed-in dust, are given by Greve (2006).

The above equations need to be complemented by dynamic and thermodynamic boundary conditions at the surface and the bottom of the respective ice body. If we assume that the surface is in contact with the atmosphere, then it can be described in good approximation as stress-free, that is,

$$\mathbf{t}\cdot\mathbf{n}|_s = \mathbf{0} \tag{10}$$

(where $\mathbf{t}$ is the full stress tensor, $\mathbf{n}$ the outer normal unit vector, and the subscript "s" denotes the surface). The surface temperature T_s can be prescribed directly as a Dirichlet condition.

If the bottom is a rigid ice/rock, ice/regolith or ice/sediment interface, no-slip conditions can be employed,

$$\mathbf{v}_b = \mathbf{0} \tag{11}$$

(the subscript "b" stands for the bottom). As for the temperature field, let us assume that the basal heat flux into the ice, $\mathbf{q}_b$, is known. This yields the Neumann condition

$$\kappa\frac{\partial T}{\partial \mathbf{n}}\bigg|_b = \mathbf{q}_b, \tag{12}$$

where $\mathbf{n}$ is again the outer normal unit vector.

The situation is different if the bottom is an ice/water interface. In this case, the basal stress conditions are governed by the hydrostatic pressure P_b of the water at the interface,

$$\mathbf{t}\cdot\mathbf{n}|_b = -P_b\mathbf{n}, \tag{13}$$

and the bottom temperature equals the pressure melting point,

$$T_b = T_m. \tag{14}$$

Provided that the role of impurities is negligible, T_m can be expressed as $T_m = T_0 - \beta P$, as already mentioned in Sect. 3.1.

3.3 Simulations for the north and south polar layered deposits

The dynamic and thermodynamic state of the present-day Martian PLDs will now be simulated with the ice-sheet model SICOPOLIS ("SImulation COde for POLythermal Ice Sheets"). This model was developed in the mid-1990's for terrestrial applications and has later been adapted to the NPLD of Mars [see Greve (2007), and references therein]. It solves the ice-flow equations described in Sect. 3.2 based on the shallow-ice approximation (Hutter 1983, Morland 1984), that is, the flow regime is assumed to be simple, bed-parallel shear, the pressure is hydrostatic and lateral shear stresses as well as normal stress deviators are neglected. Inputs from the environment are specified by the mean annual surface temperature, the net surface mass balance (ice accumulation minus ablation) and the basal ("geothermal") heat flux from the underlying lithosphere. The numerical solution of the model equations is carried out by a finite-difference integration technique.

Here we only consider steady-state conditions, that is, the ice surface is held fixed as given by the MOLA data. This is the same procedure as employed by Greve (2006), which makes it unnecessary to prescribe the surface mass balance. The topographies are shown in Figs. 5 and 6 (top left panels) for the NPLD and SPLD including their surroundings. The ice temperature, velocity and bottom topography are allowed to evolve freely until the steady state is reached. Surface temperature is parameterized by the Local Insolation Temperature (LIT) scheme (B. Grieger, pers. comm. 2004; Mahajan 2005), which uses a daily and latitude dependent radiation balance and includes a treatment of the seasonal CO_2 cap. Results agree well with those of the Martian Climate Database (Lewis et al. 1999); however, both methods fail in reproducing the observed year-round CO_2 cover of the southern residual cap. Therefore, the southern mean-annual surface temperature is corrected such that it equals the CO_2 sublimation temperature of -128°C within 85°S. The geothermal heat flux is assumed to be 35 mWm^{-2} (Schubert et al. 1992), and the source term r in the temperature evolution equation (9) is neglected.

The unknown topography of the solid ground below the PLDs is computed in two steps. First, the equilibrated ground for ice-free conditions, which is required as a reference topography, is determined by a smooth extrapolation of the ice-free ground surrounding the ice caps (Greve et al. 2004). Second, the actual ground topography is obtained by superposing the isostatic deflection (downward displacement w) of

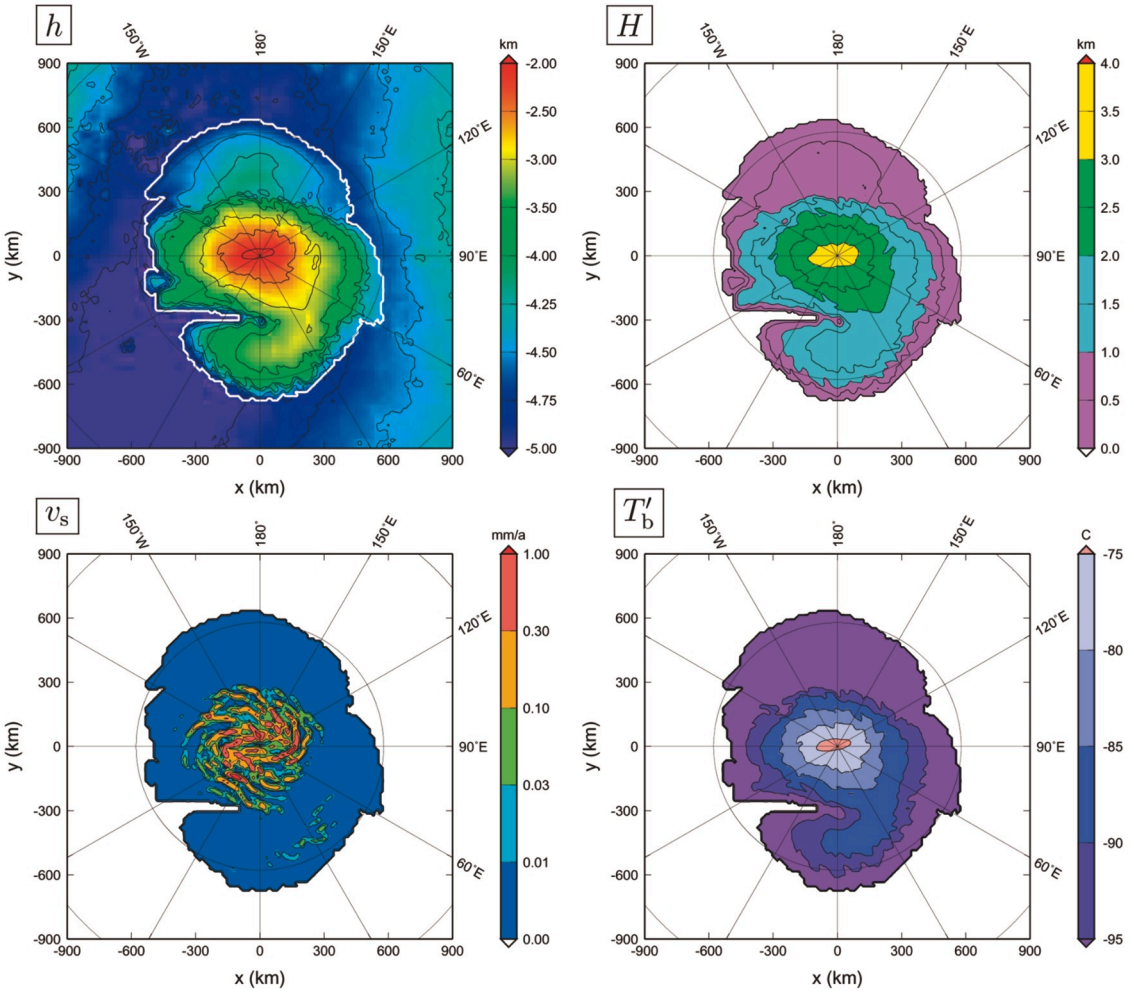

Figure 5: NPLD of Mars: MOLA surface topography h (Smith et al. 1999), computed ice thickness H, computed surface velocity v_s and computed basal temperature T'_b (relative to pressure melting) for present-day steady-state conditions. The thick white line in the surface topography plot indicates the ice margin.

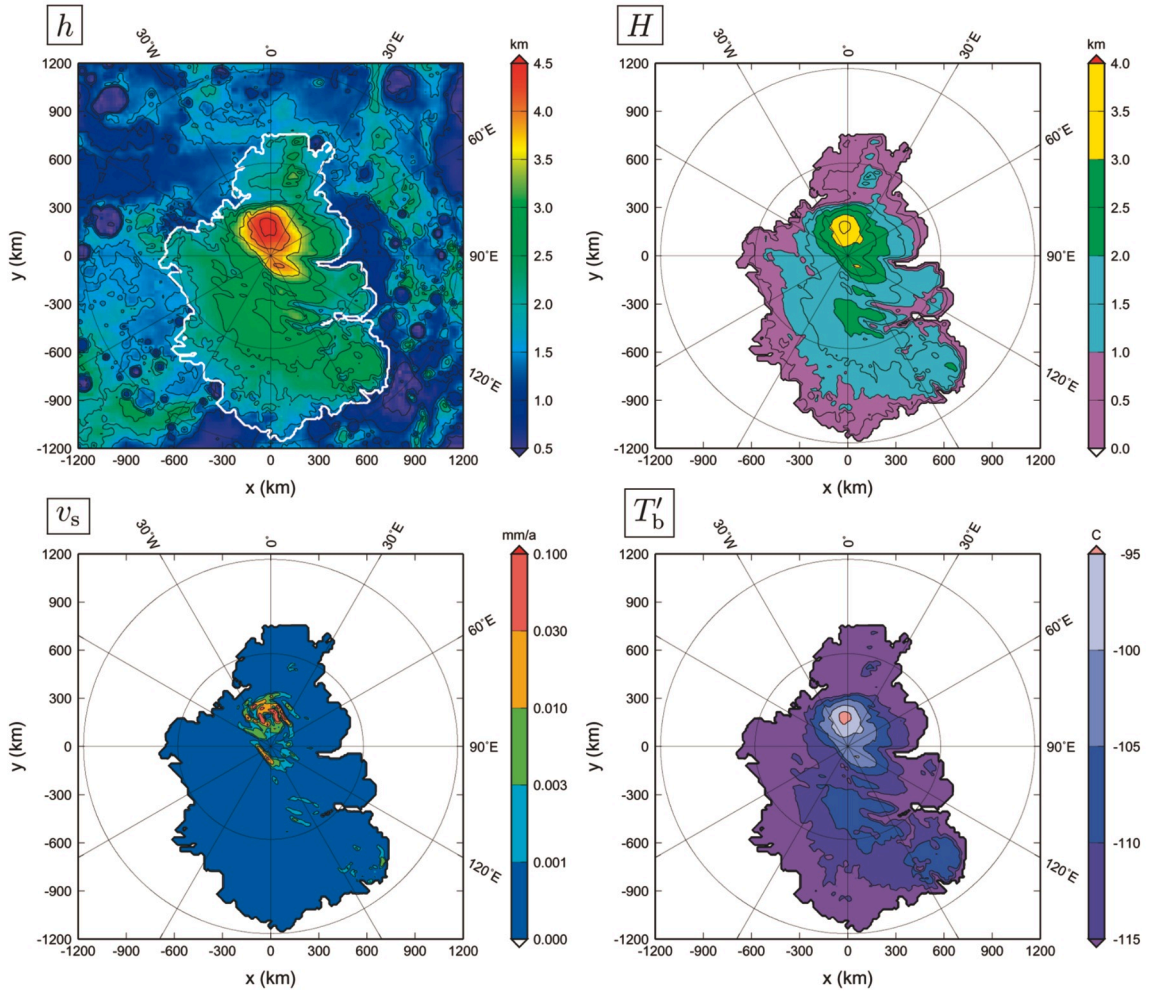

Figure 6: SPLD of Mars: MOLA surface topography h (Smith et al. 1999), computed ice thickness H, computed surface velocity v_s and computed basal temperature T'_b (relative to pressure melting) for present-day steady-state conditions. The thick white line in the surface topography plot indicates the ice margin.

the underlying lithosphere due to the ice load. By modelling the lithosphere as a thin elastic plate, the isostatic deflection is governed by the bi-potential equation

$$K_1 \nabla^4 w = \rho g H - \rho_a g w, \qquad (15)$$

where $K_1 = 3 \times 10^{25}$Nm is the flexural stiffness of the lithosphere (Greve 2007), ∇^4 the bi-potential operator in the horizontal plane and $\rho_a = 3500$kgm^{-3} the density of the asthenosphere (viscous mantle layer below the elastic lithosphere). The two load terms on the right-hand side are the ice load itself ($\rho g H$) and the counteracting buoyancy force which the deflected lithosphere experiences from the asthenosphere below ($\rho_a g w$). Note that the ice thickness H depends on w and is therefore part of the solution. In transient scenarios, which are not considered here, the elastic deflection (15) is not assumed instantaneously, so that an additional evolution equation is required for the non-equilibrium displacement (Greve 2001, Le Meur and Huybrechts 1996).

The simulations have been carried out by applying Glen's flow law as discussed in Sect. 3.1. The dust content is assumed to be 2% (Greve 2007). Horizontal resolution is 10 km in the stereographic plane with standard parallel 71°N/S, vertical resolution is 51 grid points in the cold-ice column and 11 grid points in the lithosphere column, and the time-step is 100 ka.

Results for the ice thickness, the surface velocity and the basal temperature are shown in Figs. 5 and 6 (top right and bottom panels) for both PLDs. The

NPLD assumes its maximum thickness of 3.26 km almost exactly at the pole, whereas the maximum thickness of the SPLD, 3.62 km, is offset by approx. 150 km in 10°W direction. The total volumes are 1.35×10^6 km^3 for the NPLD and 2.14×10^6 km^3 for the SPLD. Compared to terrestrial ice sheets and glaciers with typical flow velocities of tens to hundreds of meters per year, the flow of the Martian PLDs is very slow. The NPLD reaches a maximum surface velocity of 1.97 mma^{-1}, and south of 85°N surface velocities are less than 0.01 mma^{-1} almost everywhere. Therefore, the active, dynamic zone only consists of the interior, thick part of the ice cap. The situation is even more extreme for the SPLD, where the maximum surface velocity is as small as 0.11 mma^{-1}, and by far the largest part of the ice cap flows at speeds slower than a micrometer per year (note the different scales of the colour bars). Therefore, the SPLD can be considered as essentially stagnant.

Evidently, the detailed distributions of the surface velocity for both PLDs reflect the spiralling trough patterns (see Fig. 2). The largest velocities occur in the troughs which exhibit relatively steep side walls. However, the 10-km resolution applied here does not resolve the trough systems very well. Hvidberg (2003) conducted more detailed simulations at kilometer-scale horizontal resolution of a flowline of the NPLD extending from the pole in 160°E direction, and found flow velocities larger than 15 mma^{-1} in the most pronounced trough. Since this locally enhanced flow tends to close the troughs, it must be balanced by a mass exchange at the surface such that ice accumulates outside the troughs, but is removed from within them at a rate of some millimeters per year. This exchange pattern was already proposed by Fisher (1993, 2000) and termed "accublation model". Physical processes behind the "accublation" exchange are likely differential ablation due to the albedo contrast (white material outside vs. darker material inside the troughs) and/or enhanced wind erosion due to the formation of local turbulences in the troughs.

The different flow speeds of the NPLD and SPLD are mainly due to the lower ice temperatures of the SPLD, which are a consequence of the ~20°C difference in surface temperatures. Since the thicknesses of both caps are similar, and the temperature distribution is mainly controlled by heat conduction, this transfers directly to a ~20°C difference in average basal temperatures (again, note the different scales of the colour bars in the respective panels of Figs. 5 and 6). The highest basal temperatures (relative to pressure melting) are −73.9°C for the NPLD and −93.6°C for the SPLD, respectively, which demonstrates the insulating effect of the ice caps against the much colder surface temperatures. Nevertheless, the basal temperatures are in any case far below the pressure melting point. This is a very robust result, so that the presence of large amounts of subglacial liquid water as a potential habitat for Martian lifeforms seems unlikely, unless additional heat sources under the ice provide locally enhanced geothermal heat fluxes distinctly above the value of 35 mWm^{-2} used here.

4. Conclusion

We live in a Golden Age of Mars exploration. Owing to the successful orbiting and landing missions Mars Global Surveyor, Mars Pathfinder, Mars Odyssey, Mars Express, Mars Exploration Rovers Spirit/Opportunity and Mars Reconnaissance Orbiter during the last ten years, the scientific analysis of the returned data and complementary modelling work, our knowledge about the planet in general and the polar ice caps in particular has vastly expanded. The Phoenix Mars lander, which launched August 4, 2007, is scheduled to arrive on Mars on May 25, 2008. It is particularly interesting in the context of this paper because it is planned to land in the north polar region and, if this is successful, will use its robotic arm to dig a meter into the Arctic terrain (Fig. 7). The Phoenix mission has two main goals, to study the geologic history of water, the key to unlocking the story of past climate change, and to search for evidence of a habitable zone that may exist in the ice-soil boundary. So we can look forward to many exciting new data from Mars, which will further refine our understanding of the polar ice caps. Let's keep exploring!

Figure 7: Artist's conception of the Phoenix lander digging into the Martian Arctic soil (image credit: NASA).

Acknowledgements

The author wishes to thank Dr. Naoki Watanabe and Dr. Hidekazu Tanaka (ILTS) for the kind invitation to contribute this article to the current issue of *Low Temperature Science*. The simulations described in Sect. 3.3 have been carried out within the research project "Evolution and dynamics of the Martian polar ice caps over climatic cycles" funded by the ILTS.

References

Fisher, D. A. 1993. If Martian ice caps flow - ablation mechanisms and appearance. *Icarus*, **105**(2), 501–511.

Fisher, D. A. 2000. Internal layers in an "accublation" ice cap: a test for flow. *Icarus*, **144**(2), 289–294. doi: 10.1006/icar. 1999. 6293.

Forget, F. 1998. Mars CO_2 ice polar caps. In: B. Schmitt, C. de Bergh and M. Festou (Eds.), *Solar System Ices*, pp.477–507. Kluwer Academic Publishers, Dordrecht.

Greve, R. 2001. Glacial isostasy: Models for the response of the Earth to varying ice loads. In: B. Straughan, R. Greve, H. Ehrentraut and Y. Wang (Eds.), *Continuum Mechanics and Applications in Geophysics and the Environment*, pp.307–325. Springer, Berlin etc.

Greve, R. 2006. Fluid dynamics of planetary ices. *GAMM-Mitt.*, **29**(1), 29–51.

Greve, R. 2007. Scenarios for the formation of Chasma Boreale, Mars. *Icarus*. doi: 10. 1016/j. icarus. 2007.10. 020. In press.

Greve, R., R. A. Mahajan, J. Segschneider and B. Grieger. 2004. Evolution of the north-polar cap of Mars: a modelling study. *Planet. Space Sci.*, **52**(9), 775–787. doi: 10.1016/j.pss.2004.03.007.

Head, J. W., J. F. Mustard, M. A. Kreslavsky, R. E. Milliken and D. R. Marchant. 2003. Recent ice ages on Mars. *Nature*, **426**(6968), 797–802.

Herkenhoff, K. E. and J. J. Plaut. 2000. Surface ages and resurfacing rates of the polar layered deposits on Mars. *Icarus*, **144**(2), 243–253.

Hutter, K. 1983. *Theoretical Glaciology; Material Science of Ice and the Mechanics of Glaciers and Ice Sheets*. D. Reidel Publishing Company, Dordrecht, The Netherlands.

Hvidberg, C. S. 2003. Relationship between topography and flow in the north polar cap on Mars. *Ann. Glaciol.*, **37**, 363–369.

Hvidberg, C. S. 2005. Polar caps. In: T. Tokano (Ed.), *Water on Mars and Life*, pp.129–152. Springer, Berlin etc.

Kieffer, H. H. 1979. Mars south polar spring and summer temperatures: A residual CO_2 frost. *J. Geophys. Res.*, **84**, 8263–8288.

Kieffer, H. H., S. C. Chase, T. Z. Martin, E. D. Miner and F. D. Palluconi. 1976. Martian north pole summer temperatures: Dirty water ice. *Science*, **194**(4271), 13411344.

Laskar, J., A. C. M. Correia, M. Gastineau, F. Joutel, B. Levrard and P. Robutel. 2004. Long term evolution and chaotic diffusion of the insolation quantities of Mars. *Icarus*, **170**(2), 343–364. doi: 10.1016/j. icarus.2004.04.005.

Le Meur, E. and P. Huybrechts. 1996. A comparison of different ways of dealing with isostasy: examples from modelling the Antarctic ice sheet during the last glacial cycle. *Ann. Glaciol.*, **23**, 309–317.

Lewis, S. R., M. Collins, P. L. Read, F. Forget, F. Hourdin, R. Fournier, C. Hourdin, O. Talagrand and J.-P. Huot. 1999. A climate database for Mars. *J. Geophys. Res.*, **104**(E10), 24177–24194.

Mahajan, R. A. 2005. *Modelling Martian polar caps*. Doctoral thesis, University of Göttingen, Germany.

Morland, L. W. 1984. Thermo-mechanical balances of

ice sheet flows. *Geophys. Astrophys. Fluid Dyn.*, **29**, 237–266.

Nye, J. F., W. B. Durham, P. M. Schenk and J. M. Moore. 2000. The instability of a south polar cap on Mars composed of carbon dioxide. *Icarus*, **144**(2), 449–455.

Paige, D. A., K. E. Herkenhoff and B. C. Murray. 1990. Mariner 9 observations of the south polar cap of Mars: evidence for residual CO_2 frost. *J. Geophys. Res.*, **95**(B2), 1319–1335.

Paterson, W. S. B. 1994. *The Physics of Glaciers*. Pergamon Press, Oxford etc., 3rd ed.

Plaut, J. J., G. Picardi, A. Safaeinili, A. B. Ivanov, S. M. Milkovich, A. Cicchetti, W. Kofman, J. Mouginot, W. M. Farrell, R. J. Phillips, S. M. Clifford, A. Frigeri, R. Orosei, C. Federico, I. P. Williams, D. A. Gurnett, E. Nielsen, T. Hagfors, E. Heggy, E. R. Stofan, D. Plettemeier, T. R. Watters, C. J. Leuschen and P. Edenhofer. 2007. Subsurface radar sounding of the south polar layered deposits of Mars. *Science*, **316**(5821), 92–95. doi:10.1126/science.1139672.

Schubert, G., S. C. Solomon, D. L. Turcotte, M. J. Drake and N. H. Sleep. 1992. Origin and thermal evolution of Mars. In: H. H. Kieffer, B. M. Jakosky, C. W. Snyder and M. S. Matthews (Eds.), *Mars*, pp. 147–183. University of Arizona Press, Tucson.

Smith, D. E., M. T. Zuber, S. C. Solomon, R. J. Phillips, J. W. Head, J. B. Garvin, W. B. Banerdt, D. O. Muhleman, G. H. Pettengill, G. A. Neumann, F. G. Lemoine, J. B. Abshire, O. Aharonson, C. D. Brown, S. A. Hauck, A. B. Ivanov, P. J. McGovern, H. J. Zwally and T. C. Duxbury. 1999. The global topography of Mars and implications for surface evolution. *Science*, **284**(5419), 1495–1503.

Thomas, P., S. Squyres, K. Herkenhoff, A. Howard and B. Murray. 1992. Polar deposits of Mars. In: H. H. Kieffer, B. M. Jakosky, C. W. Snyder and M. S. Matthews (Eds.), *Mars*, pp.767–795. University of Arizona Press, Tucson.

Zuber, M. T., D. E. Smith, S. C. Solomon, J. B. Abshire, R. S. Afzal, O. Aharonson, K. Fishbaugh, P. G. Ford, H. V. Frey, J. B. Garvin, J. W. Head, A. B. Ivanov, C. L. Johnson, D. O. Muhleman, G. A. Neumann, G. H. Pettengill, R. J. Phillips, X. Sun, H. J. Zwally, W. B. Banerdt and T. C. Duxbury. 1998. Observations of the north polar region of Mars from the Mars Orbiter Laser Altimeter. *Science*, **282**(5396), 2053–2060.

(December 3, 2007　改訂受付)

Ralf Greve

Institute of Low Temperature Science, Hokkaido University, Kita-19, Nishi-8, Kita-ku, Sapporo 060-0819, Japan
Correspondence to: R. Greve (greve@lowtem.hokudai.ac.jp)